nature materials

ARTICLES

https://doi.org/10.1038/s41563-019-0487-0

Ionomer distribution control in porous carbon-supported catalyst layers for high-power and low Pt-loaded proton exchange membrane fuel cells

Sebastian Ott[1,6], Alin Orfanidi[2,6]*, Henrike Schmies[1], Björn Anke[3], Hong Nhan Nong[1,4], Jessica Hübner[1], Ulrich Gernert[5], Manuel Gliech[1], Martin Lerch[3] and Peter Strasser[1]*

The reduction of Pt content in the cathode for proton exchange membrane fuel cells is highly desirable to lower their costs. However, lowering the Pt loading of the cathodic electrode leads to high voltage losses. These voltage losses are known to originate from the mass transport resistance of O_2 through the platinum–ionomer interface, the location of the Pt particle with respect to the carbon support and the supports' structures. In this study, we present a new Pt catalyst/support design that substantially reduces local oxygen-related mass transport resistance. The use of chemically modified carbon supports with tailored porosity enabled controlled deposition of Pt nanoparticles on the outer and inner surface of the support particles. This resulted in an unprecedented uniform coverage of the ionomer over the high surface-area carbon supports, especially under dry operating conditions. Consequently, the present catalyst design exhibits previously unachieved fuel cell power densities in addition to high stability under voltage cycling. Thanks to the Coulombic interaction between the ionomer and N groups on the carbon support, homogeneous ionomer distribution and reproducibility during ink manufacturing process is ensured.

Even though fuel cell electric vehicles are now commercially available, even with Pt as little as 30 g per stack, it is still substantially higher than the long-term sustainable target of 5 g per vehicle[1,2]. Reducing Pt loading without sacrificing in performance, especially at the cathodic electrode, has remained a challenge over the last decade. The commonly used Pt catalysts are supported on high surface-area carbon (>800 m^2 per g of carbon) because they offer increased mass activity, which makes them highly desirable to achieve remarkable power densities even at low current densities. The increased mass activity origins from the location of the Pt particles, as a large number of Pt nanoparticles are deposited in the interior of the micropores of the carbon support and are not in direct contact with SO^{3-} groups of the ionomer. It was recently found that SO^{3-} groups of the ionomer can reduce the mass activity of pure Pt up to a factor of 3 to 4, making low surface-area carbon-supported catalysts not ideal candidates for high-power density operation[3–5]. Even though high surface-area carbon-based catalysts exhibit increased mass activity ($i_{0.9\,V}^{mass}$), referring to the current density at 0.9 V, the Pt particles in the micropores exhibit restricted protonic and reactant gas access, thus hindering performance at high current densities and dry operating conditions. Recent work from Yarlagadda et al. achieved a breakthrough by introducing a highly porous carbon Pt supported catalyst, where the pore opening of 4–7 nm resulted in catalysts that both had excellent oxygen reduction reaction (ORR) activities and transport properties, without compromising either one[6].

Recent high-resolution transmission microscopy studies showed an inhomogeneous distribution of the ionomer over the entire catalyst[7]. One approach to achieve a more homogenous distribution was recently presented by Orfanidi et al. where the carbon support was modified with surface $–NH_x$ groups promoting homogeneous ionomer distribution via Coulombic interaction with negatively charged ionomer side-chains ($–SO_3^-$) (Fig. 1a)[8]. However, the $–NH_x$ groups proved insufficiently stable to sustain the suppression of local oxygen transport losses. For this reason, in this work, we introduce a new design of high surface-area catalyst supports for Pt or Pt alloy nanoparticles to achieve sustained electrode stability, high mass activities and excellent mass transport properties in addition to a previously unachieved level of homogeneous ionomer distribution, as schematically outlined in Fig. 1b. Our approach is to introduce balanced quantities of sp^2 pyridinic/pyrrolic/graphitic N functional groups that interact with the ionomer chains, promote their homogeneous spatial distribution[9–11] and, at the same time, alter the mesoporous layer structure. As a result of this, an unprecedented uniform coverage of the proton-conducting ionomer over the high surface-area carbon supports, especially under dry operating conditions, was achieved, which resulted in previously unachieved fuel cell power densities at low Pt loading and high current densities. The presented catalyst–support pairs offer substantial advantages for the decal manufacturing process of high-performance proton exchange membrane (PEM) fuel cell electrodes.

N-modified ketjenblack carbon powder was prepared by pre-oxidizing the pristine carbon in concentrated HNO_3 at 70 °C (O-KB), followed by an ammonolysis step at elevated temperature (200, 400 and 600 °C) (Fig. 1b, details in the Supplementary Information), herein referred to as N-KB XXX °C (ref. [12]). Physicochemical characterization was conducted to identify surface and compositional changes of the different 'N-KB XXX °C' supports. Elemental analysis revealed successful N-doping of carbon with N content in the range of 0.80–1.04 at% (Table 1). Oxidation of carbon in concentrated

[1]Department of Chemistry, Chemical Engineering Division, Technical University of Berlin, Berlin, Germany. [2]BMW Group, Munich, Germany. [3]Institut für Chemie, Fachgebiet für Anorganische Festkörperchemie, Technical University of Berlin, Berlin, Germany. [4]Max Planck Institute for Chemical Energy Conversion, Mülheim an der Ruhr, Germany. [5]Center for Electron Microscopy (ZELMI), Technical University of Berlin, Berlin, Germany. [6]These authors contributed equally: Sebastian Ott, Alin Orfanidi. *e-mail: Alin.Orfanidi@bmw.de; pstrasser@tu-berlin.de

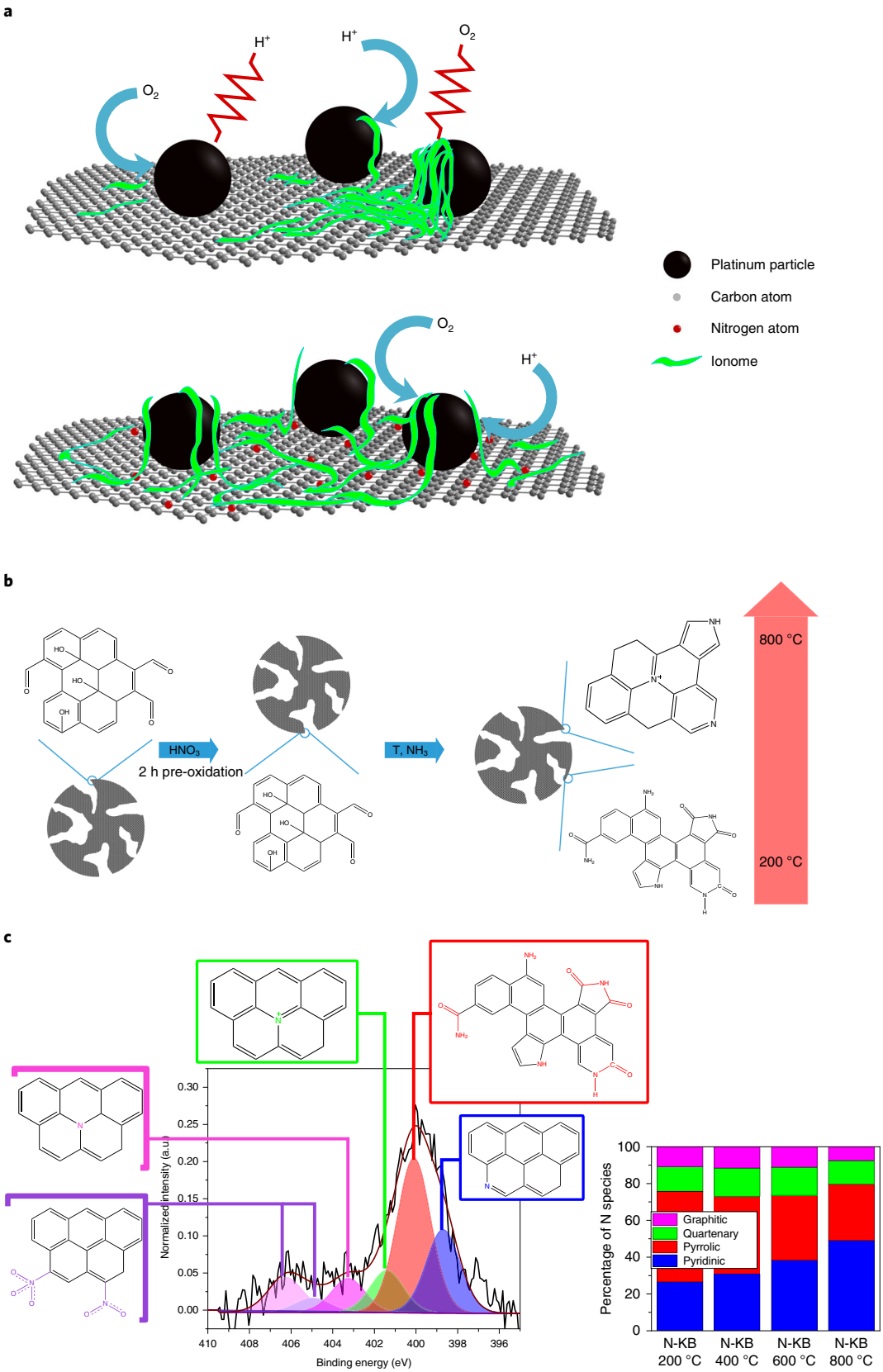

Fig. 1 | Overview of experimental approach and surface characterization. a, Schematic illustration of the ionomer distribution and thickness over the Pt/carbon surface (top) and a modified Pt/N-carbon surface (bottom) with respect to the effect of proton conductivity and O_2 mass transport. **b**, Schematic illustration of carbon (KB-EC300J) modification procedure with an initial pre-oxidation step using nitric acid, referred to as O-KB, followed by ammonolysis in pure NH_3 at 200, 400 and 600 °C, herein referred to as N-KB XXX °C. **c**, XPS N 1s spectrum of N-KB 200 °C including individual peak deconvolution of differently N-functionalized groups and a detailed overview of the fraction of these functional groups in the different heat-treated N-KB samples. N-oxide groups are not shown in the fractions' graph overview since they originate from oxidation procedure.

Table 1 | Compositional and surface analysis of the modified carbon compared to the untreated one

Sample	C (at%)	N (at%)	H (at%)	BET_{area} ($m^2 g^{-1}$)	Micro-/mesopores (—)
KB_EC300J	98.57	0	0	839 ± 6	0.72
O-KB	90.00 ± 0.00	0.11 ± 0.01	0.21 ± 0.01	-	-
N-KB 200 °C	93.48 ± 0.10	0.84 ± 0.00	0.12 ± 0.10	779 ± 34	0.76
N-KB 400 °C	95.21 ± 0.09	1.04 ± 0.10	0.13 ± 0.01	824 ± 42	0.44
N-KB 600 °C	96.45 ± 0.08	0.81 ± 0.08	0.09 ± 0.01	773 ± 16	0.64

HNO_3 leads to carboxylic, hydroxylic and NO_x groups at the surface explaining the high oxygen and small nitrogen content of O-KB (Table 1). The drastic decrease of oxygen content after ammonolysis indicates a reduction of oxygenated surface groups to nitrogenated ones[13]. The nitrogen content was maximized for N-KB 400 °C and remained comparable for N-KB 200/600 °C. However, it is known that different modification or heat treatments of the carbon can alter the meso- and microporous structure of the carbon supports. The specific surface areas (N functionalized and non-functionalized) of all support materials were determined by the Brunauer–Emmett–Teller (BET) method. To be able to differentiate changes in the meso-/microporosity as a function of NH_3 heat treatment, a detailed summary is given in Table 1. For the untreated and 200 °C treated samples, the micropore and mesopore surface ratios are 0.72 and 0.76, whereas these ratios increase for Pt/N-KB 400 °C and Pt/N-KB 600 °C up to 0.44 and 0.64, respectively. This leads to an overall higher proportion of mesoporous pores for the 400 and 600 °C treated support[14,15]. The enhanced mesoporosity is explained by carbon etching at high temperatures forming humic substances in the presence of NH_3, resulting in opening of micropores and an increase in its external surface-area[16,17]. An opened mesoporous structure is favourable for optimized mass transport as it provides better oxygen accessibility to the Pt surface and facilitates water management[6].

X-ray photoelectron spectroscopy (XPS) analysis was used to identify the different types of N group of the surface with respect to the ammonolyses temperature (Fig. 1c and Supplementary Fig. 2). Four groups of N functionalization were identified, graphitic-, quaternary-, pyrrolic- and pyridinic-N, and were deconvoluted according to their respective binding energies, as shown in Supplementary Table 3. It is clear that higher ammonolysis temperature leads to increase in pyridinic and decrease in pyrrolic groups. This shows the incorporation of N atoms into the carbon matrix instead of surface attached side-chains as it appears for low-temperature treated samples. Those changes in functionality are in good agreement with the literature assuming a decomposition of pyrrolic N to form pyridinic groups via release of HCN[18]. Such differences in N modification influence physical properties such as surface charge and thermal stability due to higher decomposition resistance. Thermogravimetric analysis (TGA) measurements confirmed an increase in thermal stability (onset of decomposition) with increase in the ammonolysis temperature of the N functionalization and the partially graphitization/decomposition of amorphous carbon during ammonolysis (Fig. 3a). A substantial enhancement in thermal stability is obtained for N-KB 600 °C compared to N-KB 200 and N-KB 400 °C. The attached $-NH_x$ groups in case of N-KB 200 °C are more labile and tend to decompose easier than incorporated N atoms. Nevertheless, the overall losses increase with N doping due to the introduction of defects, which display an imperfection or weak spot in the C matrix. One can postulate a correlation between the thermal stability and the carbon corrosion resistance under fuel cell operation, since an etching effect of stable functional groups should be less pronounced compared to weakly attached ones.

The N-modified carbons were platinized via a polyol-method, in which the carbon and Pt- precursor (H_2PtCl_6) were dispersed in ethylene glycol and reduced at 120 °C for 2 h (ref. [8]). The Pt particle size was determined by X-ray powder diffraction and TEM (see Supplementary Fig. 7 and Supplementary Table 4) and it was found to be ~2.5 nm. The nominal Pt loading of all samples was set at 16 wt% (see Supplementary Table 6 for detailed wt% Pt for each sample determined by ICP–OES). In this type of Pt deposition route, where the reducing agent is in excess and its volume is by far bigger than the volume of the pores of the carbon, it is expected that most of the Pt particles would be deposited on the external surface of the porous carbon[19]. The location of the Pt particles with respect to the carbon support internal or external surface is known to affect the mass transport of O_2 and hence the fuel cell performance[20]. To prove the Pt location on these newly synthesized catalysts, scanning electron microscopy (SEM) and TSEM (transmission SEM) images were taken simultaneously from the same area. The secondary electron signal gives information about the particles deposited on the exterior surface of the carbon support only. On the other hand, the signal of the bright field transmission electron detector shows both, the Pt particles on the exterior and interior surface. Comparing both images enables separation of the Pt particles position interior and exterior of the carbon support. As depicted in Fig. 2 the Pt distribution of roughly 85–90% exterior of the carbon is independent on the used type of carbon support (Pt/KB: 90%, Pt/N-KB 200 °C: 92% and Pt/N-KB 600 °C: 85% exterior Pt particles).

Electrochemical characterization

Thin film rotating disk electrode (RDE) ORR activity measurements were performed in the absence of ionomer on the electrode to avoid any poisoning of the Pt surface and to exclude any effects from the interaction of the carbon support with the ionomer[3–5]. Mass activities of all catalysts were found to be around 350 mA per g of Pt (g_{Pt}) at 0.9 V, thus confirming no influence of carbon support modification on intrinsic ORR activity (Fig. 3b–d). This is in perfect agreement with previously published work[8,19]. Thus, any differences in performance observed during membrane electrode assembly (MEA) characterization can be attributed to the support–ionomer interaction and changes in pore structure.

All single-cell fuel cell experiments were conducted on a 1.4 cm^2 MEA, with the exception of the dry proton accessibility measurements that we conducted in a 43.56 cm^2 MEA. For comparison reasons, all cathode layers had almost identical geometrical Pt-mass loadings (~0.11 $mg_{Pt} cm^{-2}$) and ionomer/carbon weight ratio of ~0.66, see Supplementary Table 6. Identical anodes were used in all tests with a higher Pt loading (0.15 $mg_{Pt} cm^{-2}$) to exclude any influence of the anode during the measurements. Mass activity measurements were taken at 1.4 cm^2 under constant gas flow of 1 l min^{-1} H_2 and pure O_2 of 2 l min^{-1} at 80 °C cell temperature and 100% relative humidity (RH) under 230 kPa_{abs}. Figure 4a shows the H_2/O_2 performance versus cathode Pt-mass normalized current density (in units A per g_{Pt}), corrected for HFR (high-frequency resistance) and H_2 crossover. For each catalyst type, two MEAs were manufactured and tested for reproducibility purposes, where the error bars correspond to the standard deviation between two individual measurements. The ORR mass activities were extracted at 0.9 V from Fig. 4a

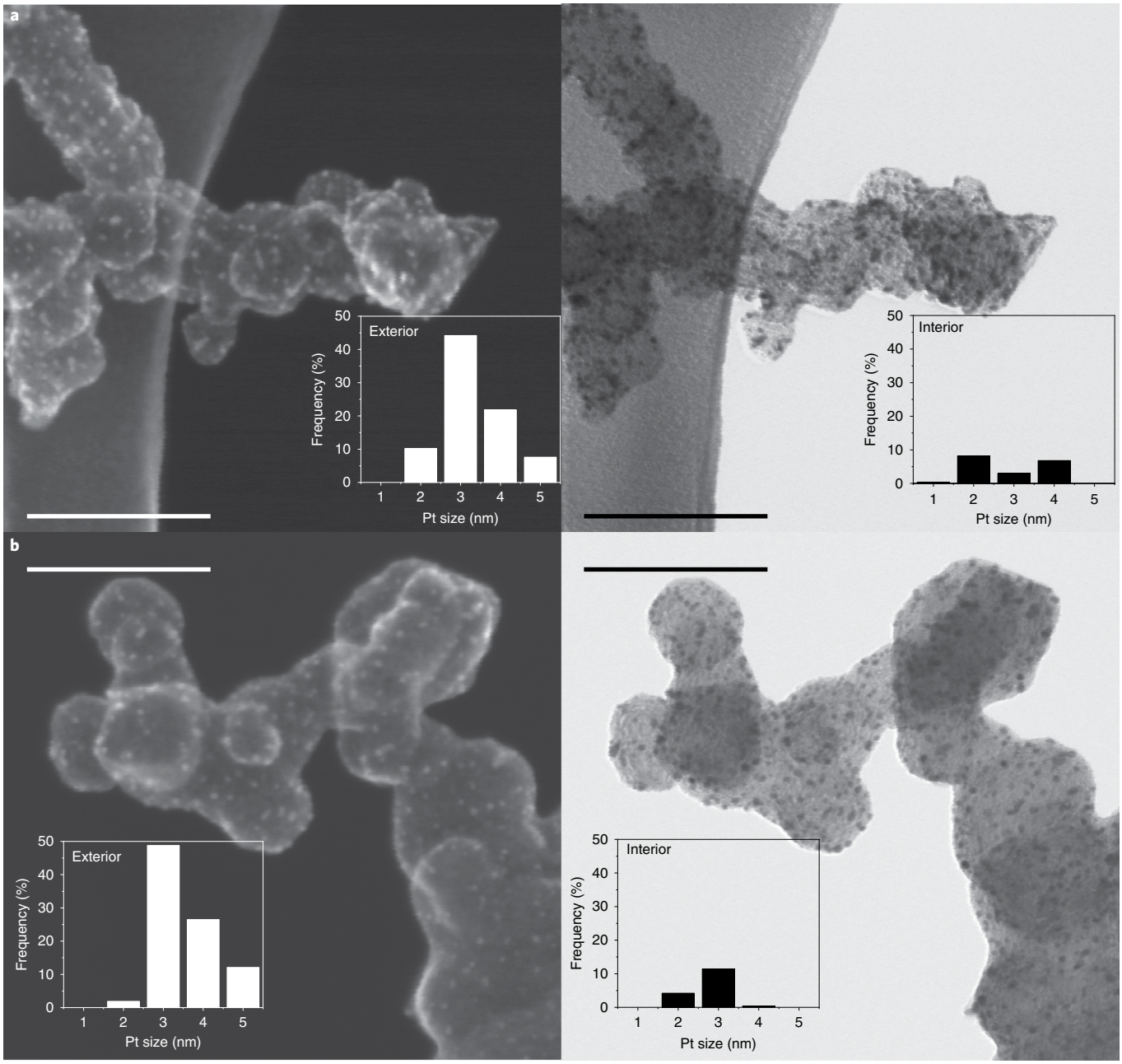

Fig. 2 | Morphological and structural characterization of catalysts synthesized in this study. Pt-particle localization of Pt/N-KB 600 °C comparing exterior and interior Pt particle applying SEM and TSEM, respectively. **a**, Pt/N-KB 600 °C. **b**, Pt/KB. The insets represent a histogram of the Pt particle size distribution exterior and interior. Scale bars, 75 nm.

and are listed in Table 2 as beginning of life (BOL = 0 cycles) mass activity. For comparison reasons, the specific activity $i^{spec}_{0.9\,V}$ is given in the Supplementary Information. These values take alteration in electrochemical surface area into account and show the same trend as mass activity data. To facilitate a better comparison with the literature, the present ORR mass activities, obtained at a total pressure of 230 kPa_{abs}, were converted to conditions of a total pressure of 150 kPa_{abs} (ref. [21]). The Tafel slopes were determined from Fig. 4a between 50 and 500 $mA\,cm^{-2}$ and are summarized in Table 2. The $i^{mass}_{0.9\,V}$ and Tafel slope of Pt/KB and Pt/N-KB 200 °C are in perfect agreement with the literature using the same carbon functionalization and Pt deposition method[19]. The obtained values of ~110–130 $A\,g^{-1}$, as for Pt/KB and Pt/N-KB 200 °C suggest that Pt particles being located primarily on the exterior surface of the carbon support. As a result of this, the Pt particles were in direct contact with the ionomer, which increased surface poisoning and depressed the experimental Pt-mass activity. On the other hand, the mass activity of the Pt/N-KB 600 °C was found to be 202 $A\,g_{Pt}^{-1}$. This would be consistent with the notion that a larger number of Pt particles were located in the porous interior of the carbon support compared to the other two types of catalyst. However, this is not entirely the case: even though TSEM data evidence show that ~85% of the Pt particles are located at the exterior (versus Pt/KB, 90% and Pt/N-KB 200 °C, 92%) this small difference does not justify the difference in the observed mass activities. This is why the mass activity increase is more plausibly explained by the expansion of mesoporous structure, as shown by BET data (Table 1), leading to a Pt deposition close to pore exits and thus minimizing the ionomer poisoning. This

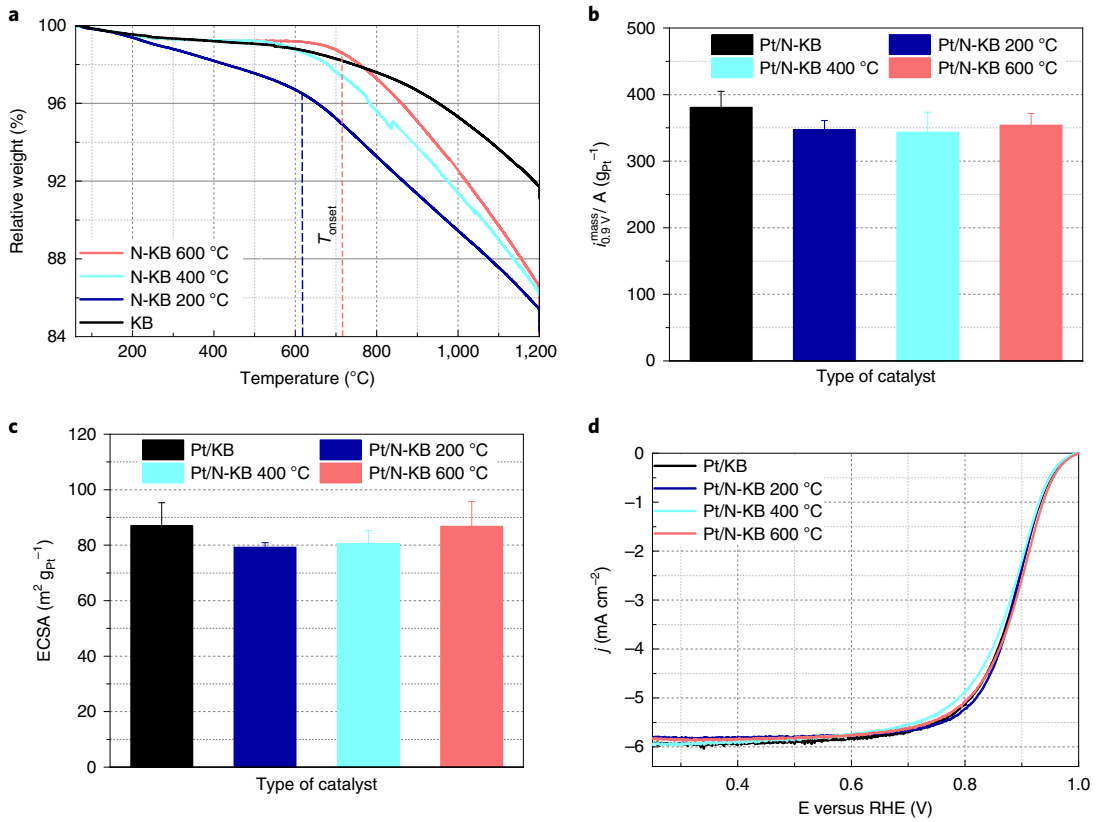

Fig. 3 | Correlation of NH3 heat treatment on thermal stability and ORR activity. a, TGA determined thermal stability of the modified and pristine carbon. Onset temperature (T_{onset}) exemplarily indicated for N-KB 200 °C and N-KB 600 °C by a vertical dashed line. **b**, Electrochemical characterization of intrinsic ORR mass activity extracted from linear sweep voltammetry (LSV) at 0.9 V. **c**, Electrochemical active surface area (ECSA) evaluation calculated from the hydrogen under potential deposition region (H_{upd}) by RDE. **d**, LSV of the different catalysts from the anodic going scan at 5 mV s^{-1} and 1,600 r.p.m. in O_2 saturated 0.1 M $HClO_4$.

enables a close contact to the ionomer for good proton conductivity but still less direct contact avoiding poisoning effects. Furthermore, this hypothesis is strengthened by the lower Tafel slopes observed for N-KB 600 °C compared to the other two catalysts, indicating better mass transport[19] due to larger mesoporous structure.

Figure 4b shows the polarization curves measured under differential flows of 21% O_2 in N_2 at 80 °C, 100% RH and 230 kPa_{abs}. It is evident that the present modified catalyst designs achieve a substantial improvement in their performance at high current densities compared to the unmodified reference catalyst. In the mass transport region, we observed a reduction in voltage losses of up to 45 mV at 2.0 A cm^{-2} by the introduction of N functions into the C matrix combined with the modification of the mesoporous structure. Using pure Pt nanoparticles, we were able to reach record power densities of up to 1.39 W cm^{-2}, previously unreported for a pure Pt catalyst. This corresponds to an effective Pt utilization of 0.075 g_{Pt} kW^{-1} on the cathode side. The benefits of the presence of N on ORR activity and performance in fuel cell have also been reported in previously published studies[22–24].

To demonstrate the outstanding performance of the Pt/N-KB 600 °C catalyst layer compared to the Pt/KB one under stoichiometric flow the corresponding polarization curves are given in Fig. 4c. After either the monopolar plate (MP) resistance R_{HFR} or the contact resistance of the MP/gas diffusion layer (GDL) $R_{MP,MP/GDL}$ corrections, a substantial overall performance increase from the modified catalyst resulted, which can be attributed to the modified catalyst/support layer itself. Particularly in the high current density region, the structural behaviour of the Pt/N-KB 600 °C catalyst layer provided beneficial transport properties resulting in sharply reduced voltage losses.

To evaluate the potential of these types of catalyst under real operating conditions, a comparison with a 43.56 cm^2 MEA under stoichiometric flow of H_2 of 1.5 and air of 2.0 at 80 °C and 100% RH is given in Supplementary Fig. 10. The voltage gap between 1.4 and 43.56 cm^2 is only observed at high current densities. This suggests that an optimized flow field and GDL to enhance mass transport in a similar way observed under differential flows will enable further improvement of the MEA performance. Nevertheless, the observed performance of the 43.56 cm^2 MEA for the N-KB 200 °C under normal stoichiometry is remarkable considering the low Pt loading.

To evaluate the ionomer distribution and the coverage over the catalyst, we evaluated the electrochemical active surface area (ECSA) via CO stripping experiments at 20% RH and 100% RH to calculate the dry proton accessibility $\left(\frac{ECSA_{RH=20}}{ECSA_{RH=100}}\right)$. The proton accessibility indicates the coverage of the ionomer and its proximity to a Pt particle (Fig. 4d). Pt/KB reveals a dry proton accessibility of around ~78%, which is lower compared to the two N-modified Pt/support couples. We can safely conclude that the lower dry proton accessibility is a result of inhomogeneous distributed ionomer, as all catalysts have almost the same percentage of Pt particles located in the external surface area of the carbon support (see Supplementary Figs. 4–6). Pt/N-KB 200 °C shows lower dry proton accessibility compared to the Pt/N-KB 600 °C, even though they both bear nitrogen functional groups that interact with the ionomer to promote its homogeneous distribution. The Pt/N-KB 600 °C has full accessibility of the Pt surface by ionomer, which, in

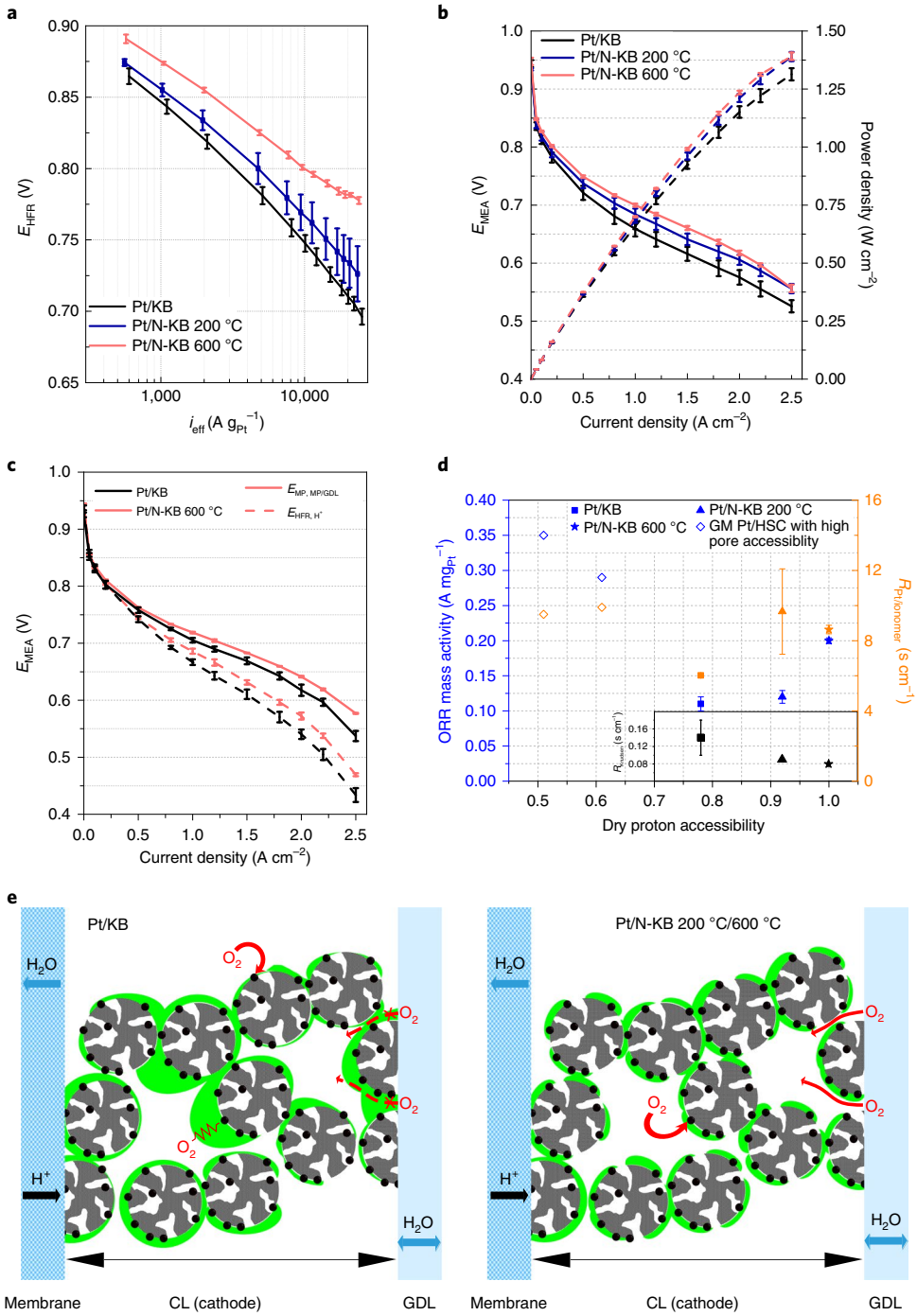

Fig. 4 | Effect of N modification on ionomer distribution and performance in fuel cell. a, Pt loading normalized performance curve of 1.4 cm^2 MEAs. **b**, H_2-air fuel cell polarization plots of 1.4 cm^2 MEAs. **c**, Comparison of 43.56 cm^2 MEA polarization curve under stoichiometric flow of 1.5 $H_2/2_{air}$, at 60 °C and $p_a = p_c = 200$ kPa$_{abs}$ and 50% RH of N-KB 600 °C (red) versus Pt/KB (black). Solid lines represent HFR-corrected polarization curves, while dashed ones only include the correction for bipolar plate and the contact resistance. **d**, ORR mass activity at 0.9 V and local O_2 transport resistance ($R_{Pt/ionomer}$) achieved from 1.4 cm^2 cells as a function of dry proton accessibility measured from 43.56 cm^2 ones. The inset reveals the Knudsen resistance ($R_{Knudsen}$) of the synthesized catalysts. For comparison reasons, two high surface carbon-based catalysts from the literature are included[6]. Conditions are set as: cathode, ~0.11 mg$_{Pt}$ cm^{-2}; anode, 0.15 mg$_{Pt}$ cm^{-2}, total outlet pressure of anode and cathode respectively $p_a = p_c = 230$ kPa$_{abs}$ under constant differential flow H_2/Air (or O_2) = 1,000/2,000 normal cubic centimetres (nccm) and the anode and cathode respectively $RH_a = RH_c = 100\%$ at 80 °C. **e**, Schematic illustration of the Knudsen resistance for oxygen transport within the catalytic layer (CL) for badly distributes ionomer layers (left) and good ionomer distribution over the entire catalyst (right).

combination with the higher $i_{0.9\,V}^{mass}$ (Fig. 4d), supports our hypothesis above that the Pt particles being deposited close to the end of pores. This is a very high level of dry proton accessibility using a high surface carbon. We attribute the proton accessibility not only to the mesoporous carbon structure, but also to the difference in the ratio of the functional groups present on the carbon surface

Table 2 | Mass activity of all catalysts used in this study under various states of degradation measured in fuel cell

	Pt/KB			Pt/N-KB 200 °C			Pt/N-KB 600 °C		
	$i^{mass}_{0.9V}$ (A g^{-1})	$i^{mass*}_{0.9V}$ (A g^{-1})	TS (mV dec)	$i^{mass}_{0.9V}$ (A g^{-1})	$i^{mass*}_{0.9V}$ (A g^{-1})	TS (mV dec^{-1})	$i^{mass}_{0.9V}$ (A g^{-1})	$i^{mass*}_{0.9V}$ (A g^{-1})	TS (mV dec^{-1})
BOL	235±21	112±10	86±2	268±20	128±9	76±4	424±10	202±4	71±1
MOL	354±79	169±37	90±4	309±14	148±7	87±1	380±16	174±7	83±1
EOL	300±63	143±30	95±6	375±64	179±30	90±5	418±21	199±10	92±0

Mass activity ($i^{mass}_{0.9V}$) measured at 230 kP$_{abs}$, recalculated[21] mass activity to an absolute O_2 pressure of 101 kPa ($i^{mass*}_{0.9V}$), and Tafel slope (TS) with units mV per decade, all determined by 1.4 cm^2 MEA measurements.

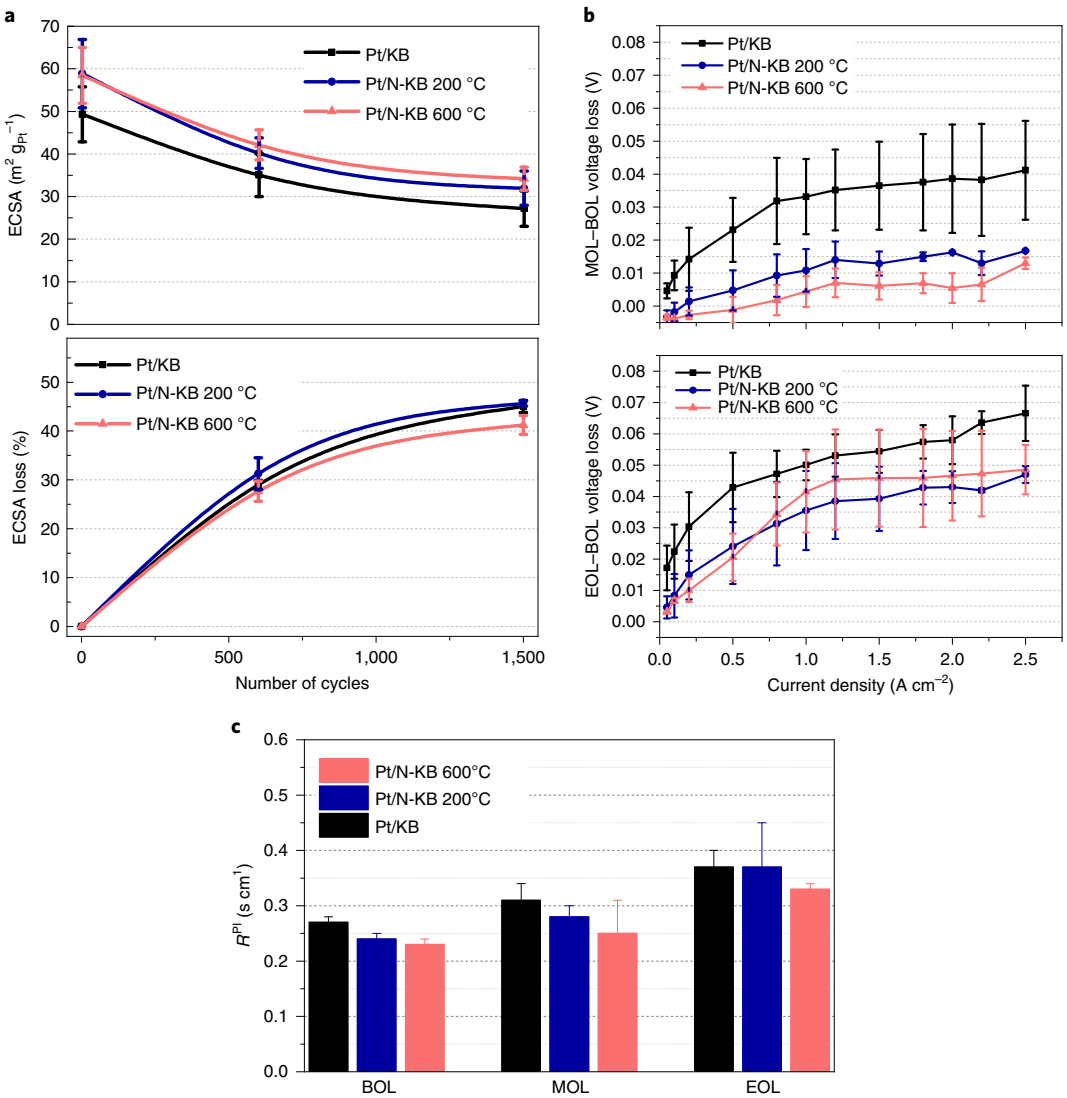

Fig. 5 | Evaluation of the stability of the N-modified catalysts under potential cycling protocol. a, Absolute (top) and relative (bottom) changes in ECSA over degradation. **b**, Voltage losses over degradation of MOL, BOL and EOL. BOL, top and bottom, respectively. BOL, MOL and EOL denote 0, 600 and 1,500 cycles of AST, respectively. Degradation follows the AST protocol at cell temperature T_{cell} = 80 °C, $RH_a = RH_c$ = 100%, $p_a = p_c$ = 101 kPa$_{abs}$ and constant flow (H_2/N_2 = 200/500 nccm) with triangular wave scanning between 0.6–1.0 V at 50 mV s^{-1}. **c**, Pressure independent parts determined at T_{cell} = 80 °C, $RH_a = RH_c$ = 100%, $p_a = p_c$ = 170–300 kPa$_{abs}$ and constant differential flow ($H_2/O_2 + N_2$ = 1,000/2,000 nccm) whereby the partial O_2 amount of O_2 diluted in N_2 varies from xO_2 = 1.5, 2, 4, 8 to 12%.

(Supplementary Fig. 2). The presence of the N functional groups alters the interaction of the ionomer with the carbon support, as each type of group would be polarized to a different extent. In addition, the nitrogen functions could also change the hydrophobicity of the carbon support, in turn affecting water management and thus RH sensitivity during ECSA measurements at 20% RH[25]. This also has important practical consequences in the context of PEM fuel cell commercialization, because a high dry proton accesibilsity

is greatly preferred in order to lower overall stack costs, as a result of reduced humidification requirements[26].

The total mass transport resistance comprises a pressure-dependent and -independent mass transport resistance. The pressure-dependent mass transport resistance (R^{PD}) is dominated by the contributions of flow field channels and the GDL. While the pressure-independent mass transport resistance term (R^{PI}) consists of the contribution of mass transport resistance dominated by Knudsen mass transport and the resistance of mass transport through the Pt–ionomer–water interface, equation (S4) in Supplementary Information (Supplementary Table 8)[11]. The local O_2 resistance of the Pt–ionomer interface of the different MEAs was plotted versus dry proton accessibility. For comparison, we have added the high surface carbon of General Motors with accessible pores, which was recently considered an important step forward in fuel cell catalyst development (Fig. 4d)[6]. As shown in Fig. 4d, Pt/KB displayed lower Pt–ionomer mass transport resistance. This is due to inhomogeneous ionomer distribution over the Pt surface, where parts of the Pt surface have remained bare and thus minimizing the total Pt–ionomer mass transport resistance. Additionally, the Knudsen resistance contribution has to be taken into consideration, which is substantially increased for poor distributed ionomer films. Since the ionomer does not cover the entire catalyst/Pt homogenously (dry proton accessibility data), it partially blocks mesopores and releases areas of thick ionomer layers over the primary carbon particle. These areas represent an additional resistance of oxygen transport through the catalytic layer (Fig. 4e)[27,28]. The Knudsen mass transport resistance, which is plotted as an inset in Fig. 4d, shows that Pt/KB exhibits the higher values. This is in perfect agreement with the inhomogeneous ionomer distribution as the micro-/mesoporous structure of the catalyst layer would be more blocked as a result of the absence of the thick, homogeneous ionomer film covering the catalyst[28]. On the other hand, the catalyst with the higher performance has a smaller Knudsen mass transport resistance, indicating, in combination with the dry proton accessibility, optimal ionomer coverage. The local Pt–ionomer resistance alone might seem contradictive to the performance data of Fig. 4a,b, but in Fig. 5c we can clearly see that Pt/KB exhibits the higher total R^{PI}, while the Pt/N-KB 600 °C has a lower value at BOL, which is in perfect agreement with the observed performance differences.

Stability under voltage cycling

To investigate the stability of the newly synthesized catalyst, the following accelerated stress test (AST) was used: voltage cycling from 0.6 V up to 1.0 V with 50 mV s^{-1} at 100% RH and cell temperature of 80 °C while flushing the anodic compartment with H_2 and the cathodic with N_2 (details in the Supplementary Information). An initial increase in mass activity over degradation is also reported in the literature but its origin is still unclear[29], whereas the increase in Tafel slope reflects a continuous degradation process due to loss in active area and pore structure (Table 2). A similar ECSA loss is observed for all catalysts after 1,500 AST cycles and is in good agreement with the literature[29], indicating no further destabilization under operation conditions by N modification (Fig. 5a). However, in the case of Pt/N-KB 600 °C the ECSA loss is slightly lowered to ~40%. Detailed analysis of voltage losses after degradation indicate a substantial enhancement of stability for the Pt/N-KB 200 °C/600 °C compared to the unmodified sample (Fig. 5b) despite similar ECSA losses for all catalysts. Although the Pt/N-KB 600 °C is the most stable one in the early stages of degradation (middle of life, MOL), it reaches similar values as the Pt/N-KB 200 °C at the end of life (EOL). One hypothesis is that the N groups act also as anchoring sites towards Pt during the Pt deposition process and do not interact only with the ionomer[30–32]. Thus, despite the ECSA reduction, our hypothesis is that the ionomer distribution remains intact over the carbon support, and voltage losses can be minimized compared to the non-functionalized carbon catalyst.

Limiting current measurements were conducted at different total outlet pressures (170, 230 and 300 kPa_{abs}) to differentiate the contributions of each component to the total mass transport resistance[33,34]. It is clearly shown in Supplementary Table 8 that the pressure dependent mass transport resistance term R_{PD} remains constant over the AST, as expected. At BOL, the triple interface resistance is substantially reduced for the N-modified samples indicating a thinner and more homogenous distributed ionomer film over the Pt particles. In the case of Pt/N-KB 600 °C, a reduced R_{PI} is achieved at BOL due to a more open pore structure.

We have presented a Pt nanoparticle/N-modified carbon support catalyst design that allowed the realization of electrode layers with highly accessible pores and a highly homogeneous ionomer distribution. Under state-of-the-art automotive single fuel cell test conditions, the Pt/N-KB 600 °C cathode catalyst showed very good stability towards voltage cycling compared to state-of-the-art reference electrodes. Our new catalyst design enabled pure Pt-based PEM cells to display power densities of up to 1.39 W cm^{-2}. Data indicated that this became possible due to Pt particles located in or close to carbon pores, lowering the degree of Pt surface poisoning by ionomer. This materials concept can be transferred to other kinds of partially amorphous carbon and is not limited to Pt as an active material. We believe that this approach would also be applicable for Pt alloys supported on carbon. What in turn would lead to even further enhanced performance due to increased activity of Pt alloys. On the basis of the performance data provided here, the introduction of heteroatom modification steps in the production line of PEM fuel cell electrocatalysts may become a path forward for wider fuel cell commercialization in automotive applications, due to enhancement in mass transport and stability, robustness of ionomer distribution and reproducibility during ink manufacturing.

Online content

Any methods, additional references, Nature Research reporting summaries, source data, statements of code and data availability and associated accession codes are available at https://doi.org/10.1038/s41563-019-0487-0.

Received: 12 April 2019; Accepted: 16 August 2019;
Published online: 30 September 2019

References

1. US DRIVE Partnership. *Fuel Cell Technical Team Roadmap, June 2013* https://energy.gov/sites/prod/files/2014/02/f8/fctt_roadmap_june2013.pdf (2013).
2. Ohma, A. et al. Analysis of proton exchange membrane fuel cell catalyst layers for reduction of platinum loading at Nissan. *Electrochimica Acta* **56**, 10832–10841 (2011).
3. Ohma, A., Fushinobu, K. & Okazaki, K. Influence of Nafion film on oxygen reduction reaction and hydrogen peroxide formation on Pt electrode for proton exchange membrane fuel cell. *Electrochimica Acta* **55**, 8829–8838 (2010).
4. Jinnouchi, R., Kudo, K., Kitano, N. & Morimoto, Y. Molecular ynamics simulations on O2 permeation through Nafion ionomer on platinum surface. *Electrochimica Acta* **188**, 767–776 (2016).
5. Shinozaki, K., Morimoto, Y., Pivovar, B. S. & Kocha, S. S. Suppression of oxygen reduction reaction activity on Pt-based electrocatalysts from ionomer incorporation. *J. Power Source.* **325**, 745–751 (2016).
6. Yarlagadda, V. C. et al. Boosting fuel cell performance with accessible carbon mesopores. *ACS Energy Lett.* **3**, 618–621 (2018).
7. Lopez-Haro, M. et al. Three-dimensional analysis of Nafion layers in fuel cell electrodes. *Nat. Commun.* **5**, 5229 (2014).
8. Orfanidi, A. et al. The key to high performance low Pt loaded electrodes. *J. Electrochem. Soc.* **164**, F418–F426 (2017).
9. Sun, L.-X. & Okada, T. Studies on interactions between Nafion and organic vapours by quartz crystal microbalance. *J. Memb. Sci.* **183**, 213–221 (2001).
10. Miyazaki, K. et al. Aminated perfluorosulfonic acid ionomers to improve the triple phase boundary region in anion exchange membrane fuel cells. *J. Electrochem. Soc.* **157**, A1153–A1157 (2010).

11. Owejan, J. P., Owejan, J. E. & Gu, W. Impact of platinum loading and catalyst layer structure on PEMFC performance. *J. Electrochem. Soc.* **160**, F824–F833 (2013).
12. Jansen, R. J. J. & van Bekkum, H. XPS of nitrogen-containing functional groups on activated carbon. *Carbon* **33**, 1021–1027 (1995).
13. Ortega, K. F., Arrigo, R., Frank, B., Schlögl, R. & Trunschke, A. Acid–base properties of N-doped carbon nanotubes: a combined temperature-programmed desorption, X-ray photoelectron spectroscopy, and 2-propanol reaction investigation. *Chem. Mat.* **28**, 6826–6839 (2016).
14. Mikhail, R. S., Brunauer, S. & Bodor, N. E. E. Investigations of a complete pore structure analysis. *J. Colloid Inter. Sci.* **26**, 45–53 (1968).
15. Lowell, S., Shields, J. E., Thomas, M. A. & Thommes, M. *Characterization of Porous Solids and Powder: Surface Area, Pore Size and Density* (Kluwer Academic, 2004).
16. Jaouen, F. & Dodelet, J.-P. Non-noble electrocatalysts for O_2 reduction: how does heat treatment affect their activity and structure? Part I. Model for carbon black gasification by NH3: parametric calibration and electrochemical validation. *J. Phys. Chem. C.* **111**, 5963–5970 (2007).
17. Sherwood, T. K., Gilliland, E. R. & Ing, S. W. Hydrogen cyanide synthesis from elements and from ammonia and carbon. *Indust. Eng. Chem.* **52**, 601–604 (1960).
18. Arrigo, R., Hävecker, M., Schlögl, R. & Su, D. S. Dynamic surface rearrangement and thermal stability of nitrogen functional groups on carbon nanotubes. *Chem. Comm.* **40**, 4891–4893 (2008).
19. Harzer, G. S., Orfanidi, A., El-Sayed, H., Madkikar, P. & Gasteiger, H. A. Tailoring catalyst morphology towards high performance for low Pt loaded PEMFC cathodes. *J. Electrochem. Soc.* **165**, F770–F779 (2018).
20. Park, Y.-C., Tokiwa, H., Kakinuma, K., Watanabe, M. & Uchida, M. Effects of carbon supports on Pt distribution, ionomer coverage and cathode performance for polymer electrolyte fuel cells. *J. Power Source.* **315**, 179–191 (2016).
21. Neyerlin, K. C., Gu, W., Jorne, J. & Gasteiger, H. A. Determination of catalyst unique parameters for the oxygen reduction reaction in a PEMFC. *J. Electrochem. Soc.* **153**, A1955–A1963 (2006).
22. Kabir, S., Artyushkova, K., Serov, A. & Atanassov, P. Role of nitrogen moieties in N-doped 3D-graphene nanosheets for oxygen electroreduction in acidic and alkaline media. *ACS App. Mat. Int.* **10**, 11623–11632 (2018).
23. Lai, L. et al. Exploration of the active center structure of nitrogen-doped graphene-based catalysts for oxygen reduction reaction. *Energy Environ. Sci.* **5**, 7936 (2012).
24. Yang, S. et al. Efficient synthesis of heteroatom (N or S)-doped graphene based on ultrathin graphene oxide-porous silica sheets for oxygen reduction reactions. *Adv. Funct. Mat.* **22**, 3634–3640 (2012).
25. Artyushkova, K. et al. Role of surface chemistry on catalyst/ionomer interactions for transition metal–nitrogen–carbon electrocatalysts. *ACS Appl. Energy Mat.* **1**, 68–77 (2017).
26. Ohma, A. et al. Membrane and catalyst performance targets for automotive fuel cells by FCCJ membrane. *ECS Trans.* **41**, 775–784 (2011).
27. Kongkanand, A. & Mathias, M. F. The priority and challenge of high-power performance of low-platinum proton-exchange membrane fuel cells. *J. Phys. Chem. Lett.* **7**, 1127–1137 (2016).
28. Orfanidi, A., Rheinlander, P. J., Schulte, N. & Gasteiger, H. A. Ink solvent dependence of the ionomer distribution in the catalyst layer of a PEMFC. *J. Electrochem. Soc.* **165**, F1254–F1263 (2018).
29. Harzer, G. S., Schwammlein, J. N., Damjanovic, A. M., Ghosh, S. & Gasteiger, H. A. Cathode loading impact on voltage cycling induced PEMFC degradation: a voltage loss analysis. *J. Electrochem. Soc.* **165**, F3118–F3131 (2018).
30. Schmies, H. et al. Impact of carbon support functionalization on the electrochemical stability of Pt fuel cell catalysts. *Chem. Mater.* **30**, 7287–7295 (2018).
31. Zhou, Y. et al. Enhancement of Pt and Pt-alloy fuel cell catalyst activity and durability via nitrogen-modified carbon supports. *Energy Environ. Sci.* **3**, 1437–1446 (2010).
32. Shi, W. et al. Enhanced stability of immobilized platinum nanoparticles through nitrogen heteroatoms on doped carbon supports. *Chem. Mater.* **29**, 8670–8678 (2017).
33. Baker, D. R. C. C. A., Neyerlin, K. C. & Murph, M. W. Measurement of oxygen transport resistance in PEM fuel cells by limiting current methods. *J. Electrochem. Soc.* **156**, B991–B1003 (2009).
34. Caulk, D. A. & Baker, D. R. Heat and water transport in hydrophobic diffusion media of PEM fuel cells. *J. Electrochem. Soc.* **157**, B1237–B1244 (2010).

Acknowledgements

This work was supported by the BMW Group. We also thank the members of FC Test Field, FC Technology Development and Technology Material Analysis of BMW Group for their support during fuel cell testing, MEA manufacturing and decal preparation.

Author contributions

A.O. conceived the project. S.O. synthesized all the samples. S.O. and A.O. carried out the MEA manufacturing, fuel cell experiments and data analysis. H.S. and B.A. contributed to material synthesis including ammonolysis. H.N.N. conducted and analysed XPS measurements. J.H. conducted and analysed nitrogen physisorption measurements. U.G. carried out SEM/STEM measurements. M.G. carried out TGA measurements. P.S. provided guidance and constructive ideas throughout the project to ensure the successful outcome of this project. All authors contributed to the discussion part, drew conclusions and participated in finalizing the text and figures.

Competing interests

The authors declare no competing interests.

Additional information

Supplementary information is available for this paper at https://doi.org/10.1038/s41563-019-0487-0.

Correspondence and requests for materials should be addressed to A.O. or P.S.

Reprints and permissions information is available at www.nature.com/reprints.

Publisher's note Springer Nature remains neutral with regard to jurisdictional claims in published maps and institutional affiliations.

© The Author(s), under exclusive licence to Springer Nature Limited 2019

Methods

Material synthesis. Commercial carbon ketjenblack EC-300J (AkzoNobel) was mixed with 100 ml 70% HNO_3 and continuously stirred under reflux for 2 h in a 70 °C pre-heated oil bath. Thereafter, the preoxidized carbon was ammonolysed in a tube furnace under constant NH_3 flow at 200, 400 or 600 °C. The oven was ramped up to a set temperature (T_{set} °C) with a heating rate of 400 K h^{-1} and held for 2.5 h. Then 16 wt% Pt/N-KB XXX°C was synthesized depositing Pt on the initial or modified carbon via polyol-method. Then, 300 mg of the functionalized carbon was mixed with 200 ml of ethylene glycol, 100 ml of deionized water and 1.35 ml of an H_2PtCl_6 0.25 mol l^{-1} solution. The dispersion first was stirred for 18 h at 25 °C and then for 2 h under reflux conditions at 120 °C.

Characterization. Elemental analysis was determined by a Thermo Flash 1112 Organic Elemental Analyzer after decomposition in a $WO_3/Cu/Al_2O_3$ reactor. N_2 physisorption was carried out in an Autosorb-1 (Quantachrome) at 77 K applying the BET method and slit/cylindrical pore adsorption QSDFT kernel (quenched solid density functional theory) for evaluation of micro and mesoporosity. Thermogravimetric analysis of all the carbon supports was performed using a TGA-DSC PerkinElmer STA-8000. Determination of the chemical surface composition of the different carbon supports was carried out in ultrahigh vacuum at room temperature using a non-monochromatized Al Kα (1,486.6 eV) excitation and a hemispherical analyser (Phoibos 150, SPECS). The catalyst was characterized using a Bruker D8 Advance diffractometer with a single beam and a source of Cu Kα1 (characteristic wavelenth $\lambda = 1.54051$ Å). SEM was conducted for simultaneous surface and transmission imaging by use of a Hitachi SU8030 SEM with a cold field emitter cathode operated at a 30 kV acceleration voltage.

Electrochemical measurement. All measurements were taken in a 0.1 M $HClO_4$ using a mercury or mercury sulfate reference electrode and a Pt mesh as the counter electrode. To control the potential of the working electrode, a SP-150 or SP-200 potentiostat (BioLogic Instruments) was used. The catalyst inks were prepared by adding roughly 7 mg of catalyst mixed with H_2O/isopropanol resulting in a solution of 1.4 mg_{cat} ml^{-1}. After 15 min of ice-bath sonification, a droplet of 10 µl of ink was placed on a 5 mm diameter gas chromatography electrode representing the working electrode. Cyclic voltammograms were recorded in a range between 0.05 V and 1 V versus reversible hydrogen electrode (RHE) at 20 mV s^{-1} after initial conditioning of 50 cycles between 0.05 and 1 V versus RHE. ORR activity were extracted from 5 mV s^{-1} anodic scan at 1,600 r.p.m. deriving the mass activity at 0.9 V. All values have been corrected for mass transport and resistances originating from the electrolyte and contact resistances (*iR* corrected) in the RDE cell.

MEA preparation and electrochemical measurement. All MEAs were fabricated using the decal transfer method. Catalyst inks were prepared by mixing the catalyst with low EW ionomer solution (725 EW dry powder dispersed in 40% H_2O/60% 1-propanol) and a specific water/1-propanol ratio (see Supplementary Information). The cathode loading was 0.105 mg_{Pt} cm^{-2} and the anode one 0.15 mg_{Pt} cm^{-2} using 19.7 wt% Pt/graphitized-ketjenblack. The electrochemical measurements were performed using a modified single-cell hardware from Tandem Technologies containing a 50 cm^2 active area. The active area of the tested MEAs was tuned to 1.4 and 43.56 cm^2. After activation and recovery of the 1.4 and 43.56 cm^2 cells at 80 °C, CO stripping was conducted adsorbing CO (1% CO in N_2 and 200 nccm) for 30 min at 80 °C and 101 kPa_{abs}. Cyclic voltammogram from 0.053 V up to 1.2 V_{RHE} with a scan rate of 50 mV s^{-1}, was performed to remove the adsorbed CO. In the case of 43.56 cm^2 MEA, the relative humidity was altered (20% RH and 100% RH) to make it possible to calculate the dry proton accessibility. Pol curves of 1.4 cm^2 MEAs were recorded at 80 °C and 100% RH applying a backpressure of 230 $kPa_{abs,out}$, while keeping the flow of the reacting gas H_2/air (or O_2) constant at 1,000/2,000 nccm, respectively. At each current density, the respective HFR was recorded using a Hioki at 1 kHz. Evaluation of the mass transport resistance was evaluated from limiting current measurements at 80 °C and 100% RH under differential flows (1,000 nccm of H_2 and 2,000 nccm O_2/N_2). The dry oxygen mole fractions used were 1.5, 2, 4, 8 and 12% O_2 in N_2. All measurements were conducted at 170, 230 and 300 kPa_{abs}. The run AST was subjected to a triangular wave voltage cycling protocol (applied by Zahner, IM6) between 0.6 and 1.0 V with a scan rate of 50 mV s^{-1}. The cell temperature was set at 80 °C and 100% RH. During the AST, the backpressure of the anodic and cathodic compartment was set at ambient pressure (101 $kPa_{abs,out}$). The H_2 flow was set at 500 nccm, while the flow at the cathodic compartment was set at 500 nccm of N_2.

Data availability

The data supporting the findings of this study are available within this article and its Supplementary Information files, or from the corresponding author upon reasonable request. The Supplementary Information contains descriptions of methods, discussion on physicochemical characterization and the electrochemical characterization of as-prepared/conducted CO stripping, polarization curves, limiting current measurements and accelerated stress testing. It also includes Supplementary Figs. 1–12 and Supplementary Tables 1–8.